Monthly Notices
of the
ROYAL ASTRONOMICAL SOCIETY

Mon. Not. R. Astron. Soc. **422,** 1988–1998 (2012) doi:10.1111/j.1365-2966.2012.20635.x

WASP-44b, WASP-45b and WASP-46b: three short-period, transiting extrasolar planets

D. R. Anderson,[1⋆] A. Collier Cameron,[2] M. Gillon,[3] C. Hellier,[1] E. Jehin,[3] M. Lendl,[4] P. F. L. Maxted,[1] D. Queloz,[4] B. Smalley,[1] A. M. S. Smith,[1] A. H. M. J. Triaud,[4] R. G. West,[5] F. Pepe,[4] D. Pollacco,[6] D. Ségransan,[4] I. Todd[6] and S. Udry[4]

[1]*Astrophysics Group, Keele University, Staffordshire ST5 5BG*
[2]*SUPA, School of Physics and Astronomy, University of St Andrews, North Haugh, Fife KY16 9SS*
[3]*Institut d'Astrophysique et de Géophysique, Université de Liège, Allée du 6 Août, 17, Bat. B5C, Liège 1, Belgium*
[4]*Observatoire de Genève, Université de Genève, 51 Chemin des Maillettes, 1290 Sauverny, Switzerland*
[5]*Department of Physics and Astronomy, University of Leicester, Leicester LE1 7RH*
[6]*Astrophysics Research Centre, School of Mathematics & Physics, Queen's University, University Road, Belfast BT7 1NN*

Accepted 2012 January 21. Received 2012 January 21; in original form 2011 May 15

ABSTRACT

We report the discovery of three extrasolar planets that transit their moderately bright (m_V = 12–13) host stars. WASP-44b is a 0.89-M_{Jup} planet in a 2.42-day orbit around a G8V star. WASP-45b is a 1.03-M_{Jup} planet which passes in front of the limb of its K2V host star every 3.13 days. Weak Ca II H&K emission seen in the spectra of WASP-45 suggests that the star is chromospherically active. WASP-46b is a 2.10-M_{Jup} planet in a 1.43-day orbit around a G6V star. Rotational modulation of the light curves of WASP-46 and weak Ca II H&K emission in its spectra show the star to be photospherically and chromospherically active.

We imposed circular orbits in our analyses as the radial-velocity data are consistent with (near-)circular orbits, as could be expected from both empirical and tidal-theory perspectives for such short-period, ∼Jupiter-mass planets. We discuss the impact of fitting for eccentric orbits for such planets when not supported by the data. The derived planetary and stellar radii depend on the fitted eccentricity and these parameters inform intense theoretical efforts concerning tidal circularization and heating, bulk planetary composition and the observed systematic errors in planetary and stellar radii. As such, we recommend exercising caution in fitting the orbits of short-period, ∼Jupiter-mass planets with an eccentric model when there is no evidence of non-circularity.

Key words: planets and satellites: individual: WASP-44b – planets and satellites: individual: WASP-45b – planets and satellites: individual: WASP-46b – stars: individual: WASP-44 – stars: individual: WASP-45 – stars: individual: WASP-46.

1 INTRODUCTION

The ensemble of well-characterized transiting extrasolar planets is growing at pace, with well over 100 known to date. It is important to determine the system parameters accurately so that the inferences based on them are reliable. For example, to determine the bulk composition of a planet it is necessary to measure accurately its radius (e.g. Fortney, Marley & Barnes 2007). Many short-period, giant planets (e.g. WASP-17b; Anderson et al. 2010, 2011b) are larger than predicted by standard cooling theory of irradiated, gas-giant planets (e.g. Fortney et al. 2007). One potential explanation is that energy from the tidal circularization of eccentric orbits was dissipated within the planets' interiors, causing them to bloat (e.g. Bodenheimer, Lin & Mardling 2001). To evaluate the likelihood that a planet was inflated by such tidal heating, it is necessary to have an accurate determination of both its radius and its orbital eccentricity (e.g. Ibgui, Spiegel & Burrows 2011).

A planet's orbital eccentricity can be determined by measuring the radial motion of its host star around its orbit (e.g. Queloz et al. 2010), or by observing occultations of the planet by its host star (e.g. Anderson et al. 2011b), or from a combination of the two. By combining this eccentricity measurement with high-quality transit light curves, we can measure a star's density (Seager & Mallén-Ornelas 2003). The stellar mass can be estimated using stellar evolution models (e.g. Demarque et al. 2004) or mass-calibration laws (e.g. Torres, Andersen & Giménez 2010), and the stellar radius follows. This, combined with the ratio of the radii derived from the transit depth, gives the planet radius.

⋆E-mail: dra@astro.keele.ac.uk

© 2012 The Authors
Monthly Notices of the Royal Astronomical Society © 2012 RAS

In papers announcing new planet discoveries, eccentricity is often poorly determined, thus the planet radius can be uncertain. Despite this, there are theoretical (Goldreich & Soter 1966) and empirical (Pont et al. 2011) reasons to expect short-period ($\lesssim$4 d), Jupiter-mass ($\approx$0.5–2 $M_{\rm Jup}$) planets, often referred to as *hot Jupiters*, to be in circular orbits. Thus, it is reasonable, in the absence of evidence to the contrary, to assume that a newly discovered hot Jupiter is in a circular orbit. In so doing, the derived stellar and planetary dimensions will be, on the whole, accurate.

In this paper we present three new hot Jupiters, WASP-44b, WASP-45b and WASP-46b, and discuss the effects of fitting an eccentric orbit model to a hot-Jupiter system in the absence of evidence for non-circularity.

2 OBSERVATIONS

2.1 Discovery photometry

The Wide Area Search for Planets (WASP) photometric survey (Pollacco et al. 2006) employs two eight-camera arrays, each with a field of view of 450 deg^2, to monitor bright stars ($m_{\rm V}$ = 8–15). Each array observes up to eight pointings per night with a cadence of 5–10 min, and each pointing is followed for around five months at a time. The WASP-South station (Hellier et al. 2011) is hosted by the South African Astronomical Observatory in South Africa and the SuperWASP-North station (Faedi et al. 2011b) is hosted by the Observatorio del Roque de Los Muchachos on La Palma. The WASP data were processed and searched for transit signals as described in Collier Cameron et al. (2006) and the candidate selection process is described in Collier Cameron et al. (2007).

WASP-44 is a $m_{\rm V}$ = 12.9, G8V star located in the constellation Cetus. A transit search of the light curve obtained by WASP-South from 2009 July to November found a weak, 2.42-d periodicity. Further observations in 2008 and 2009 with both WASP instruments led to a total of 15 755 photometric measurements (Fig. 1).

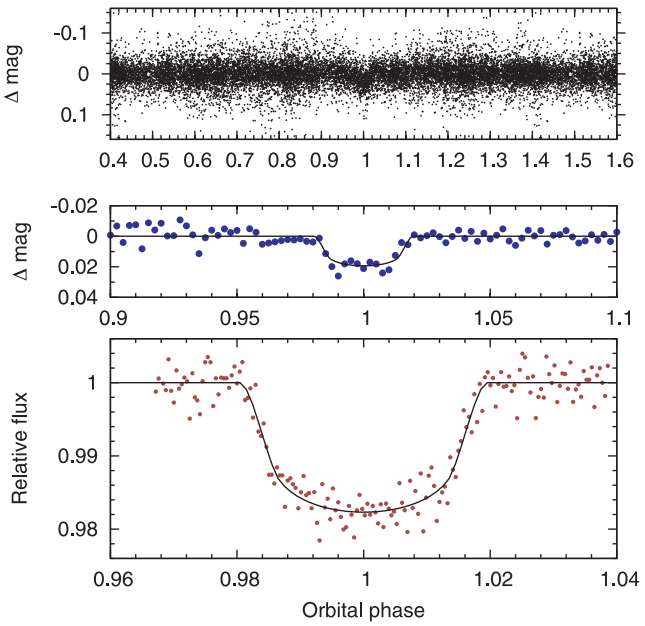

Figure 1. Photometry of WASP-44, with the best-fitting transit model superimposed. Top: WASP discovery light curve, folded on the ephemeris of Table 6. Middle: WASP data around the transit, binned in time with a bin width of ~9 min. Bottom: high-precision transit light curve from Euler.

WASP-44 was also observed by a SuperWASP-North camera during 2010 August to November. The resulting light curve comprises 6000 measurements and became available during the preparation of this paper. As such, it was not used in determination of the system parameters (Section 4), but was used in the search for rotational modulation (Section 5).

WASP-45 is a $m_{\rm V}$ = 12.0, K2V star located in the constellation Sculptor that was observed by WASP-South during 2006 May to November and 2007 May to November. A transit search of the resulting light curve, which comprises 11 007 photometric measurements, found a strong 3.13-d periodicity (Fig. 2).

WASP-46 is a $m_{\rm V}$ = 12.9, G6V star located in the constellation Indus that was observed by two WASP-South cameras during 2008 May to October and 2009 May to October. A transit search of the resulting light curve, which comprises 41 961 photometric measurements, found a strong 1.43-d periodicity (Fig. 3). WASP-46 was also observed by two WASP-South cameras during 2010 August to November. The resulting light curve comprises 19 000 measurements and became available during the preparation of this paper. As such, it was not used in the determination of the system parameters (Section 4), but was used in the search for rotational modulation (Section 5).

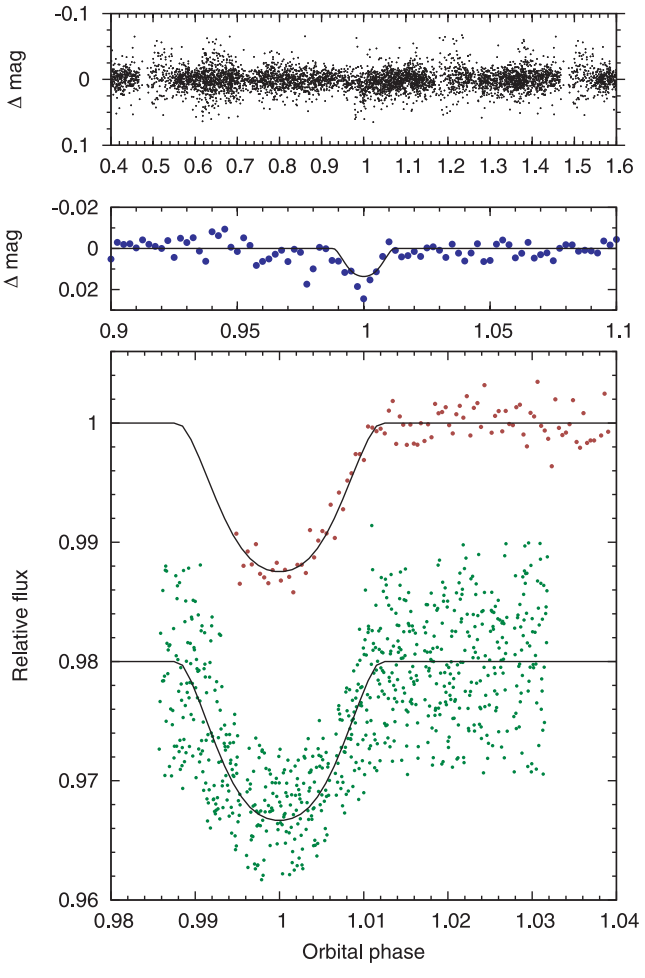

Figure 2. Photometry of WASP-45, with the best-fitting transit model superimposed. Top: WASP discovery light curve, folded on the ephemeris of Table 6. Middle: WASP data around the transit, binned in time with a bin width of ~11 min. Bottom: high-precision transit light curves from Euler (upper) and TRAPPIST (lower).

© 2012 The Authors, MNRAS **422,** 1988–1998
Monthly Notices of the Royal Astronomical Society © 2012 RAS

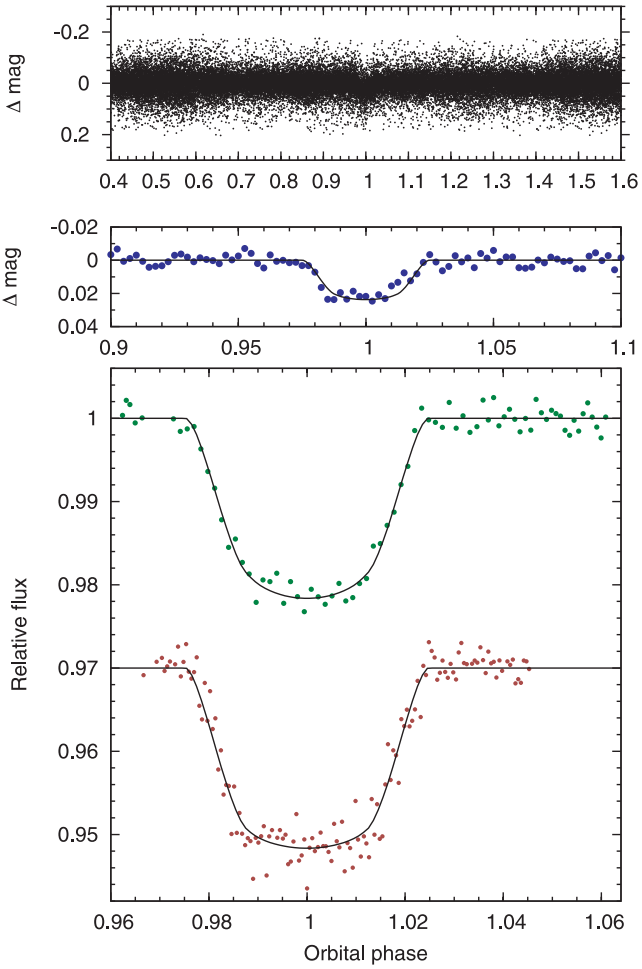

Figure 3. Photometry of WASP-46, with the best-fitting transit model superimposed. Top: WASP discovery light curve, folded on the ephemeris of Table 6. Middle: WASP data around the transit, binned in time with a bin width of ∼5 min. Bottom: high-precision transit light curves from TRAPPIST (upper) and Euler (lower).

WASP-46 is blended in the WASP images with a $m_V = 14.8$ star at a separation of 17.4 arcsec (the plate scale is 13.7 arcsec pixel^{-1} and the photometry aperture has a radius of 3.5 pixel). We corrected the WASP photometry for this contamination to prevent dilution of the transit.

2.2 Spectroscopic follow-up

In 2010 we used the CORALIE spectrograph mounted on the 1.2-m Euler-Swiss telescope (Baranne et al. 1996; Queloz et al. 2000) to obtain spectra of the three target stars. We obtained 17 spectra of WASP-44, 13 spectra of WASP-45 and 16 spectra of WASP-46. Radial-velocity (RV) measurements were computed by weighted cross-correlation (Baranne et al. 1996; Pepe et al. 2005) with a numerical G2-spectral template for both WASP-44 and WASP-46, and with a K5-spectral template for WASP-45. RV variations were detected with the same periods found from the WASP photometry and with semi-amplitudes consistent with planetary-mass companions. The RV measurements are listed in Table 1 and are plotted separately for each system in Figs 4–6. We excluded two RVs of WASP-44 from the analysis as the spectra were taken during transit and we do not fit for the Rossiter–McLaughlin effect (e.g. Simpson et al. 2011).

Table 1. Radial-velocity measurements.

Star	BJD (UTC) (d)	RV (km s^{-1})	σ_{RV} (km s^{-1})	BS (km s^{-1})
WASP-44	245 5378.8533	−4.114	0.028	−0.063
WASP-44	245 5387.7850	−3.923	0.019	−0.011
WASP-44	245 5388.9089	−4.173	0.024	−0.020
WASP-44	245 5389.7778	−3.894	0.040	−0.191
WASP-44	245 5390.7802[a]	−4.074	0.025	0.006
WASP-44	245 5391.8691	−4.095	0.020	−0.156
WASP-44	245 5392.7604	−3.905	0.023	−0.038
WASP-44	245 5396.8995	−4.033	0.039	−0.013
WASP-44	245 5414.8075	−3.981	0.020	−0.026
WASP-44	245 5446.8271	−4.149	0.027	−0.065
WASP-44	245 5448.9128[a]	−4.013	0.032	−0.005
WASP-44	245 5449.8568	−4.173	0.024	−0.012
WASP-44	245 5450.8095	−3.912	0.025	0.001
WASP-44	245 5451.8089	−4.162	0.025	−0.059
WASP-44	245 5453.6439	−3.999	0.018	−0.017
WASP-44	245 5454.8482	−4.049	0.026	−0.069
WASP-44	245 5482.6600	−3.978	0.025	−0.096
WASP-45	245 5388.9353	4.406	0.010	−0.044
WASP-45	245 5390.8149	4.680	0.012	0.030
WASP-45	245 5391.8937	4.414	0.011	0.016
WASP-45	245 5392.8314	4.552	0.010	0.012
WASP-45	245 5393.7593	4.704	0.014	0.013
WASP-45	245 5404.8466	4.426	0.010	−0.035
WASP-45	245 5410.7215	4.392	0.019	−0.048
WASP-45	245 5414.7627	4.557	0.015	−0.011
WASP-45	245 5446.8614	4.683	0.012	−0.024
WASP-45	245 5449.8794	4.699	0.011	0.018
WASP-45	245 5451.8550	4.452	0.015	−0.000
WASP-45	245 5453.8741	4.507	0.011	−0.004
WASP-45	245 5482.6826	4.410	0.013	0.033
WASP-46	245 5334.8428	−3.414	0.029	−0.044
WASP-46	245 5359.8870	−4.116	0.033	−0.014
WASP-46	245 5382.7544	−4.092	0.062	0.158
WASP-46	245 5385.8357	−3.869	0.032	−0.016
WASP-46	245 5389.8330	−4.144	0.024	−0.075
WASP-46	245 5390.6889	−3.491	0.036	−0.074
WASP-46	245 5391.7867	−3.516	0.026	0.057
WASP-46	245 5392.6562	−4.183	0.031	0.010
WASP-46	245 5396.7744	−4.058	0.026	−0.033
WASP-46	245 5400.6822	−3.382	0.027	0.009
WASP-46	245 5409.6251	−4.025	0.028	0.005
WASP-46	245 5413.5695	−3.555	0.033	0.082
WASP-46	245 5414.8452	−3.433	0.047	0.115
WASP-46	245 5445.6578	−4.141	0.024	−0.092
WASP-46	245 5449.7606	−4.090	0.036	0.047
WASP-46	245 5454.7010	−3.513	0.026	−0.083

[a]These two RVs were excluded from the analysis as they were measured during transit.

For each system we tested the hypothesis that the RV variations are due to spectral-line distortions caused by a blended eclipsing binary or star spots by performing a line-bisector analysis (Queloz et al. 2001) of the CORALIE cross-correlation functions. The lack of correlation between bisector span and RV (Figs 4–6) supports our conclusion that the periodic dimming and RV variation of each system are caused by a transiting planet.

2.3 Follow-up photometry

We obtained high signal-to-noise ratio (S/N) transit photometry to refine the parameters of each system. We used the 1.2-m

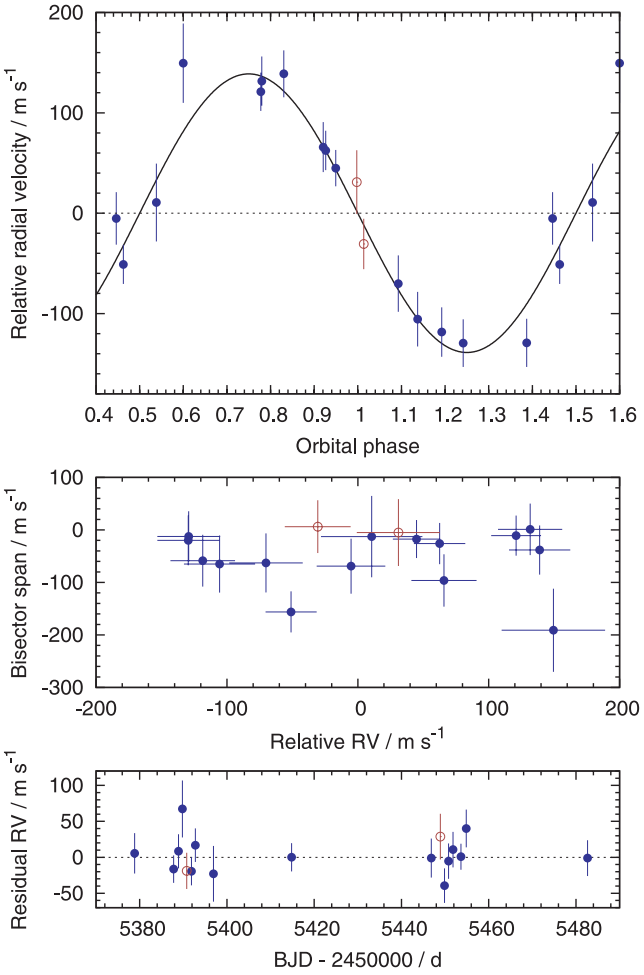

Figure 4. Top: CORALIE RVs of WASP-44 with the best-fitting circular Keplerian orbit superimposed (rms = 25.0 m s^{-1}, χ^2 = 10.9). The RVs represented by open, red circles were excluded from the analysis as they were taken during transit. Middle: bisector span with respect to RV. We adopted uncertainties on the bisector spans twice the size of those on the RVs. Bottom: residuals of the RVs about the fit as a function of time.

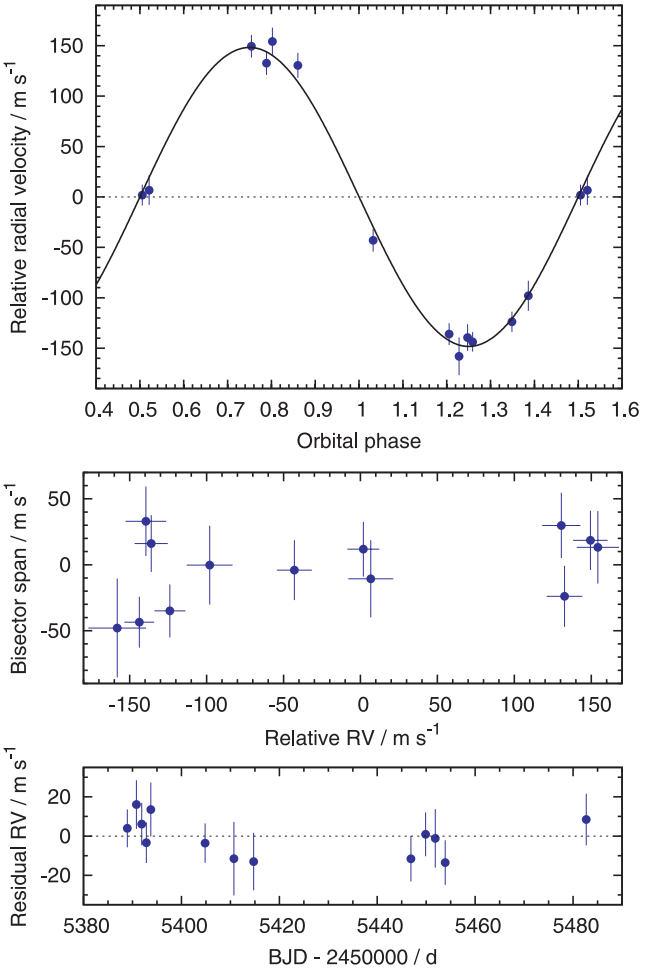

Figure 5. Top: CORALIE RVs of WASP-45 with the best-fitting circular Keplerian orbit superimposed (rms = 9.7 m s^{-1}, χ^2 = 7.4). Middle: bisector span with respect to RV. We adopted uncertainties on the bisector spans twice the size of those on the RVs. Bottom: residuals of the RVs about the fit as a function of time.

Euler-Swiss telescope located at European Southern Observatory (ESO) La Silla Observatory, Chile to observe one transit each of WASP-44b, WASP-45b and WASP-46b. Observations were made through a Gunn *r* filter and Euler's absolute tracking mode was used to keep the stars on the same location on the chip. This is done by calculating an astrometric solution for each science frame and adjusting the telescope pointing between exposures. After correcting the images for bias, overscan and flat-field variations, we extracted aperture photometry for the bright stars in the field. We selected the aperture radius and set of reference stars that resulted in the smallest light-curve residuals.

We used TRAPPIST,[1] a 60-cm robotic telescope also located at ESO La Silla (Gillon et al. 2011) to observe one transit of WASP-45b and one transit of WASP-46b. Both transits were observed through a special $I+z$ filter, in the 2-MHz readout mode, and with 1×1 binning, resulting in a typical combined readout and overhead time of 8 s and a readout noise of 13.5 e$^-$. The 'software guiding' system of TRAPPIST kept the stars at the same positions on the chip to within a few pixels over the course of the observations (Gillon et al., in preparation).

[1] TRAnsiting Planets and PlanetesImals Small Telescope; http://arachnos.astro.ulg.ac.be/Sci/Trappist.

2.3.1 *WASP-44b*

A transit of WASP-44b was observed on 2010 September 14 by Euler. We observed for a total of 4.2 h, from 46 min before the start of the transit to 65 min after it ended. The conditions were clear, airmass ranged from 1.04 to 1.44 and no defocus was applied. The WASP-44b transit light curve is shown in Fig. 1 and the data are given in Table 2.

2.3.2 *WASP-45b*

A partial transit of WASP-45b was observed on 2010 September 11 by Euler. We observed for a total of 3.3 h, from partway through the transit to 2 h after it ended. The seeing was poor (1–2 arcsec) and airmass ranged from 1.01 to 1.22. We applied a defocus of 0.1 mm to increase the duty cycle and to minimize pixel-to-pixel effects.

A transit of WASP-45b was observed on 2010 December 17 by TRAPPIST. Observations lasted from 00:15 to 03:40 h UT, during

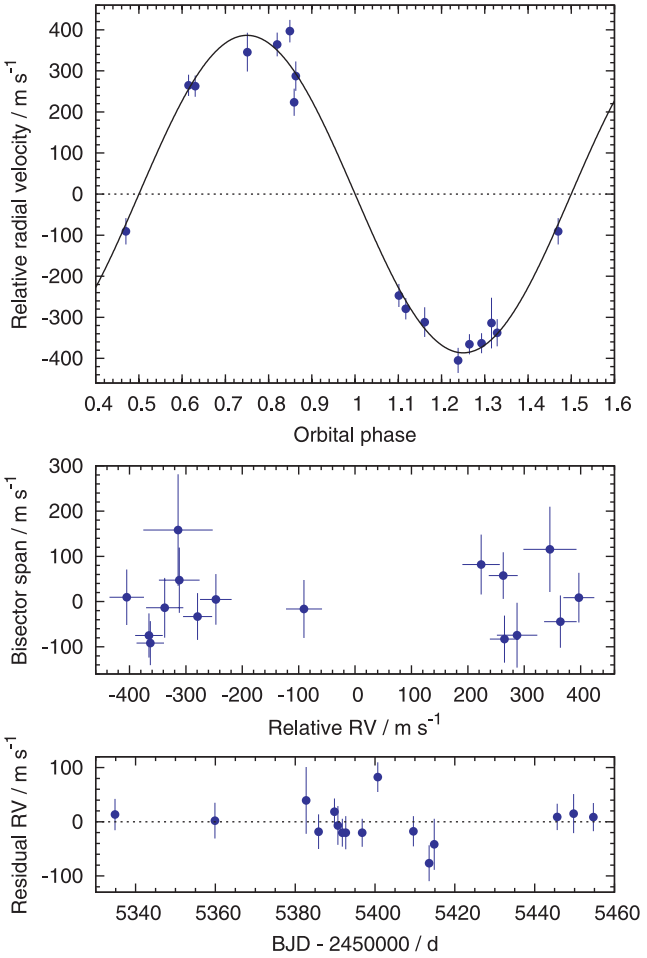

Figure 6. Top: CORALIE RVs of WASP-46 with the best-fitting circular Keplerian orbit superimposed (rms = 34.2 m s^{-1}, $\chi^2 = 19.2$). Middle: bisector span with respect to RV. We adopted uncertainties on the bisector spans twice the size of those on the RVs. Bottom: residuals of the RVs about the fit as a function of time.

Table 2. Euler and TRAPPIST photometry of the three stars.

Set	Star	Telescope	BJD (UTC) −245 0000	Rel. flux	ΔRel. flux
1	WASP-44	Euler	5453.686 865	0.9989	0.0015
1	WASP-44	Euler	5453.687 942	1.0007	0.0015
1	WASP-44	Euler	5453.689 683	1.0000	0.0015
...	...	...	...	...	...
5	WASP-46	Euler	5449.614 796	0.9991	0.0014
5	WASP-46	Euler	5449.616 092	0.9978	0.0014
5	WASP-46	Euler	5449.617 396	1.0003	0.0014

This table is available in its entirety in the online journal (see Supporting Information).

which the airmass increased from 1.03 to 1.73 and the transparency was good. The telescope was strongly defocused to average pixel-to-pixel sensitivity variations and to increase the duty cycle, resulting in a typical full width at half-maximum (FWHM) of the stellar images of ∼9 pixel (∼5.8 arcsec). The integration time was 6 s. After a standard pre-reduction (bias, dark and flat-field correction), the stellar fluxes were extracted from the images using the IRAF/DAOPHOT[2] aperture photometry software (Stetson 1987). We tested several sets of reduction parameters and chose the set that gave the most precise photometry for the stars of similar brightness to WASP-45. We carefully selected a set of reference stars and then performed differential photometry.

The WASP-45b transit light curves are shown in Fig. 2 and the data are given in Table 2.

2.3.3 *WASP-46b*

A transit of WASP-46b was observed on 2010 July 19 by TRAPPIST. Observations lasted from 01:15 to 04:05 h UT , during which the airmass decreased from 1.83 to 1.22 and the transparency was good. Considering the relative faintness of the target, we chose to keep the telescope focused during the run, and we used an integration time of 60 s. The pre-reduction and reduction procedures were similar to those used for the WASP-45 data.

A transit of WASP-46b was observed on 2010 September 10 by Euler. We observed for a total of 3.4 h, from 35 min before the start of transit to 75 min after it ended. The conditions were variable and airmass increased from 1.12 to 1.4 during the observations. No defocus was applied.

The WASP-46b transit light curves are shown in Fig. 3 and the data are given in Table 2.

3 STELLAR PARAMETERS FROM SPECTRA

For each system, the CORALIE spectra were co-added to produce a single spectrum with a typical S/N of around 50:1. The analysis was performed using the methods given in Gillon et al. (2009). The Hα line was used to determine the effective temperature ($T_{\rm eff}$), while the Na I D and Mg I b lines were used as surface gravity ($\log g_*$) diagnostics. The parameters obtained from the analysis are given in Table 3. The elemental abundances were determined from equivalent width measurements of several clean and unblended lines. A value for microturbulence ($\xi_{\rm t}$) was determined from Fe I using the method of Magain (1984). The quoted error estimates include that given by the uncertainties in $T_{\rm eff}$, $\log g_*$ and $\xi_{\rm t}$, as well as the scatter due to measurement and atomic data uncertainties.

The projected stellar rotation velocities ($v \sin I$) were determined by fitting the profiles of several unblended Fe I lines. For this we used an instrumental FWHM of 0.11 ± 0.01 Å (= 5.2 ± 0.5 km s^{-1}), determined from the telluric lines around 6300 Å (equating to a spectral resolution of ∼57 000), and used the Bruntt et al. (2010) calibration to assume values for macroturbulence ($v_{\rm mac}$). The $v_{\rm mac}$ values we assumed were 1.4 ± 0.3 km s^{-1} for WASP-44, 0.7 ± 0.3 km s^{-1} for WASP-45 and 2.0 ± 0.3 km s^{-1} for WASP-46.

Though the S/N values are very low in the Ca II H&K regions of our spectra, we searched for signs of emission, which would be indicative of stellar chromospheric activity. The WASP-44 spectra show no signs of emission and both the WASP-45 and WASP-46 spectra show weak emission.

We input our values of $T_{\rm eff}$, $\log g_*$ and [Fe/H] into the calibrations of Torres et al. (2010) to obtain estimates of the stellar mass and radius.

We used the method of Barnes (2007) to estimate gyrochronological ages for the stars. For WASP-44 and WASP-45 we calculated

[2] IRAF is distributed by the National Optical Astronomy Observatory, which is operated by the Association of Universities for Research in Astronomy, Inc., under cooperative agreement with the National Science Foundation.

Table 3. Stellar parameters from spectra.

Parameter (unit)	WASP-44	WASP-45	WASP-46
$T_{\rm eff}$ (K)	5400 ± 150	5100 ± 200	5600 ± 150
$\log g_*$ (CGS)	4.5 ± 0.2	4.4 ± 0.2	4.4 ± 0.2
$\xi_{\rm t}$ (km s^{-1})	1.0 ± 0.2	0.5 ± 0.3	1.0 ± 0.2
$v \sin I$ (km s^{-1})	3.2 ± 0.9	2.3 ± 0.7	1.9 ± 1.2
[Fe/H]	0.06 ± 0.10	0.36 ± 0.12	-0.37 ± 0.13
[Na/H]	0.24 ± 0.09	0.56 ± 0.14	-0.35 ± 0.09
[Mg/H]	0.25 ± 0.07	0.57 ± 0.09	-0.10 ± 0.10
[Al/H]	0.20 ± 0.13	0.45 ± 0.11	-0.24 ± 0.08
[Si/H]	0.25 ± 0.13	0.50 ± 0.15	-0.27 ± 0.10
[Ca/H]	0.10 ± 0.17	0.38 ± 0.17	-0.21 ± 0.13
[Sc/H]	0.30 ± 0.17	0.45 ± 0.27	-0.13 ± 0.16
[Ti/H]	0.12 ± 0.10	0.46 ± 0.20	-0.29 ± 0.18
[V/H]	0.24 ± 0.17	0.73 ± 0.18	-0.21 ± 0.21
[Cr/H]	0.13 ± 0.07	0.34 ± 0.12	-0.31 ± 0.12
[Mn/H]	0.29 ± 0.10	0.93 ± 0.24	-0.47 ± 0.14
[Co/H]	0.23 ± 0.09	0.70 ± 0.11	-0.32 ± 0.24
[Ni/H]	0.13 ± 0.12	0.51 ± 0.16	-0.39 ± 0.10
$\log A$(Li)[a]	<1.0	<0.8	<0.8
M_* ($M_\odot$)	0.95 ± 0.08	0.95 ± 0.10	0.93 ± 0.09
R_* ($R_\odot$)	0.90 ± 0.22	1.00 ± 0.25	1.00 ± 0.26
Spec. type	G8V	K2V	G6V
Gyro. age	$0.9^{+1.0}_{-0.6}$	$1.4^{+2.0}_{-1.0}$	$1.4^{+0.4}_{-0.6}$
RA (J2000)	$00^{\rm h}15^{\rm m}36\overset{\rm s}{.}76$	$00^{\rm h}20^{\rm m}56\overset{\rm s}{.}99$	$21^{\rm h}14^{\rm m}56\overset{\rm s}{.}86$
Dec. (J2000)	$-11^\circ 56' 17\overset{''}{.}4$	$-35^\circ 59' 53\overset{''}{.}8$	$-55^\circ 52' 18\overset{''}{.}1$
$m_{\rm V}$	12.9	12.0 ± 0.2	12.9
$m_{\rm J}$[b]	11.70 ± 0.02	10.75 ± 0.02	11.75 ± 0.02
$m_{\rm H}$[b]	11.41 ± 0.03	10.37 ± 0.03	11.47 ± 0.03
$m_{\rm K}$[b]	11.34 ± 0.03	10.29 ± 0.02	11.40 ± 0.03
2MASS[b]	00153675−1156172	00205699−3559537	21145687−5552184

[a] $\log A({\rm Li}) = \log N({\rm Li/H}) + 12$, where N(Li/H]) is the number density of lithium with respect to hydrogen.
[b] Skrutskie et al. (2006).

rotation periods from our $v \sin I$ determinations. If either star is inclined with respect to the sky plane then it will be rotating faster than suggested by $v \sin I$ and so is likely to be younger than indicated. For WASP-46, the rotation period found from the modulation of the WASP light curves was used (see Section 5). As such, the age estimate for this star is not just an upper limit.

4 SYSTEM PARAMETERS FROM RV AND TRANSIT DATA

4.1 WASP-44b and WASP-46b

We determined the parameters of each system from a simultaneous fit to all data. The fit was performed using the current version of the Markov chain Monte Carlo (MCMC) code described by Collier Cameron et al. (2007) and Pollacco et al. (2008).

The transit light curves were modelled using the formulation of Mandel & Agol (2002) with the assumption that the planet is much smaller than the star. Limb darkening was accounted for using a four-coefficient, non-linear limb-darkening model, using coefficients appropriate to the passbands from the tabulations of Claret (2000, 2004). The coefficients were interpolated once using the values of $\log g_*$ and [Fe/H] in Table 3, but were interpolated at each MCMC step using the latest value of $T_{\rm eff}$. The coefficient values corresponding to the best-fitting value of $T_{\rm eff}$ are given in Table 4. The transit light curve is parametrized by the epoch of mid-transit T_0, the orbital period P, the planet-to-star area ratio $(R_{\rm pl}/R_*)^2$, the approximate duration of the transit from initial to final contact T_{14} and the impact parameter $b = a \cos i/R_*$ (the distance, in fractional stellar radii, of the transit chord from the star's centre in the case of a circular orbit), where a is the semimajor axis and i is the inclination of the orbital plane with respect to the sky plane.

The eccentric Keplerian RV orbit is parametrized by the stellar reflex velocity semi-amplitude K_1, the systemic velocity γ, and $\sqrt{e}\cos\omega$ and $\sqrt{e}\sin\omega$ (Collier Cameron, in preparation), where e is orbital eccentricity and ω is the argument of periastron.

The linear scale of the system depends on the orbital separation a which, through Kepler's third law, depends on the stellar mass M_*. At each step in the Markov chain, the latest values of ρ_*, $T_{\rm eff}$ and [Fe/H] are input into the empirical mass calibration of Enoch et al. (2010) to obtain M_*. The shapes of the transit light curves and the RV curve constrain ρ_* (Seager & Mallén-Ornelas 2003), which combines with M_* to give R_*. $T_{\rm eff}$ and [Fe/H] are proposal parameters constrained by Gaussian priors with mean values and variances derived directly from the stellar spectra (see Section 3).

As the planet–star area ratio is determined from the measured transit depth, $R_{\rm pl}$ follows from R_*. The planet mass $M_{\rm pl}$ is calculated from the measured value of K_1 and the value of M_*; the planetary density $\rho_{\rm pl}$ and surface gravity $\log g_{\rm pl}$ then follow. We calculate the planetary equilibrium temperature $T_{\rm eql}$, assuming zero albedo and efficient redistribution of heat from the planet's presumed permanent day side to its night side. We also calculate the durations of transit ingress (T_{12}) and egress (T_{34}), the total occultation duration (T_{58}), and the durations of occultation ingress (T_{56}) and egress (T_{78}).

Table 4. Limb-darkening coefficients.

Planet	Instrument	Observation bands	Claret band	a_1	a_2	a_3	a_4
WASP-44	WASP/Euler	Broad (400–700 nm)/Gunn r	Cousins R	0.646	−0.437	1.080	−0.519
WASP-45	WASP/Euler	Broad (400–700 nm)/Gunn r	Cousins R	0.755	−0.768	1.450	−0.623
WASP-45	TRAPPIST	Cousins I+Sloan z'	Sloan z'	0.833	−0.891	1.304	−0.547
WASP-46	WASP/Euler	Broad (400–700 nm)/Gunn r	Cousins R	0.543	−0.055	0.592	−0.348
WASP-46	TRAPPIST	Cousins I+Sloan z'	Sloan z'	0.630	−0.371	0.727	−0.366

At each step in the MCMC procedure, model transit light curves and RV curves are computed from the proposal parameter values, which are perturbed from the previous values by a small, random amount. The χ^2 statistic is used to judge the goodness of fit of these models to the data and a step is accepted if χ^2 is lower than for the previous step. A step with higher χ^2 is accepted with a probability proportional to $\exp(-\Delta\chi^2/2)$, which gives the procedure some robustness against local minima and leads to the thorough exploration of the parameter space around the best-fitting solution. To give proper weighting to each photometry data set, the uncertainties were scaled at the start of the MCMC so as to obtain a photometric reduced χ^2 of unity. For the same reason, a jitter term of 10.2 m s^{-1} was added in quadrature to the formal errors of the WASP-46 RVs. A possible source of this jitter is stellar activity, as indicated by chromospheric and photometric indicators (Sections 3 and 5). With reduced spectroscopic χ^2 values of less than unity, it was not necessary to add any jitter to the RVs of WASP-44.

4.2 WASP-45b

The analysis for WASP-45b was the same as for WASP-44b and WASP-46b, except we used evolutionary models to impose priors on stellar mass and density for reasons to be explained.

The apparent lack of the second and third contact points in the transit light curves of WASP-45b (Fig. 2) indicates that the transit is grazing or near-grazing. When $b + R_{\rm pl}/R_* > 1$, the planet does not fully pass in front of the star. Thus, as b tends towards higher values, $R_{\rm pl}$ must inflate so that the ratio $R_{\rm pl}/R_*$ remains consistent with the observed transit depth. Also, R_* must inflate so as to remain consistent with the observed transit duration. This results in stellar and planetary radii that are non-physical in a sizeable portion of accepted MCMC steps.

To avoid biasing the derived stellar and planetary radii to larger values, we imposed a prior on stellar density using the constraints provided by our gyrochronological age determination (Table 3) and evolutionary models. Our gyrochronolgical age is determined using $v \sin I$ and so is an upper limit. If the stellar spin axis is inclined with respect to the sky plane then the star will truly be rotating faster and will therefore be younger. We plotted the isochrones and mass tracks of Demarque et al. (2004) relevant to the value ranges we obtained for $T_{\rm eff}$, [Fe/H] and age (Fig. 7). By interpolating the models for these measured values, we obtained stellar dimensions consistent with the models: $\rho_* = 1.65 \pm 0.40\ \rho_\odot$ and $M_* = 0.91 \pm 0.06\ {\rm M}_\odot$. We used these values to place Gaussian priors, by means of Bayesian penalties on χ^2, at each MCMC step.

It was not necessary to add any jitter to the RVs of WASP-45.

4.3 The imposition of circular orbits

For each system, the best-fitting eccentricity is small and consistent with zero (Table 5). We used the F-test approach of Lucy & Sweeney (1971) to calculate the probability, $\mathbb{P}_{\rm LS}$, that the improvement in the fit that results from fitting for an eccentric orbit could have arisen by chance if the underlying orbit were circular. For each system, we found $\mathbb{P}_{\rm LS}$ to be much higher (Table 5) than the threshold of 0.05 suggested by Lucy & Sweeney (1971), below which they consider the detection of a non-zero eccentricity to be significant. In the absence of conclusive evidence to the contrary, we assumed the orbit of each planet to be circular in producing the adopted solutions that we present. This issue is dealt with at greater length in the discussion.

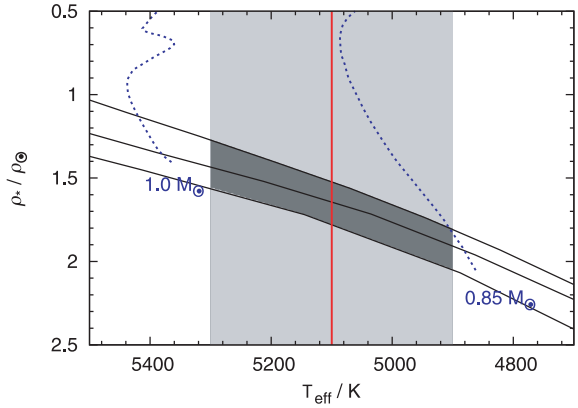

Figure 7. Evolutionary diagram for WASP-45 with the models of Demarque et al. (2004). The solid, black lines are isochrones, with the ages coming from gyrochronology: [Fe/H] = 0.48 and 3.4 Gyr (top); [Fe/H] = 0.36 and 1.4 Gyr (middle); and [Fe/H] = 0.24 and 0.4 Gyr (bottom). The two dashed, blue lines are the mass tracks for 1.0 M$_\odot$ with [Fe/H] = 0.48 and 0.85 M$_\odot$ with [Fe/H] = 0.24. The isochrones and mass tracks we chose to display are those that bound the region of interest, which is the area shaded dark grey that indicates the range of stellar densities consistent with the models. The solid, red line indicates our best-fitting $T_{\rm eff}$, and the area shaded light grey corresponds to the 1σ confidence interval.

4.4 Results

The median values and 1σ uncertainties of the system parameters derived from the MCMC model fits are presented in Table 6. The corresponding transit models are superimposed on the transit photometry in Figs 1–3. The corresponding orbit models are superimposed on the RVs in Figs 4–6, in which we also show the RV residuals as a function of time. From the residual plots one can evaluate both the level to which stellar activity may have affected the RVs and the evidence for a third body. The RVs of each planet-hosting star, obtained over the course of 100 days, show no evidence for motion induced by a third body. The residuals of WASP-46 show greater scatter ($\chi^2 = 19.2$ for WASP-46 compared to 10.9 for WASP-44 and 7.4 for WASP-45), which is probably due to the star being active (see Sections 3 and 5).

We also performed MCMCs fitting an eccentric model to the RVs so as to illustrate the impact on those parameters that are liable to be

Table 5. The limits placed on orbital eccentricity and the impact of fitting for it.

Parameter (unit)	WASP-44	WASP-45	WASP-46
$\mathrm{rms}_{\mathrm{spec}}$ ($\mathrm{m\,s^{-1}}$)	24.8	8.8	33.9
χ^2_{spec}	10.5	6.3	18.1
e	$0.036^{+0.054}_{-0.025}$	$0.023^{+0.027}_{-0.016}$	$0.018^{+0.021}_{-0.013}$
$\mathbb{P}_{\mathrm{LS}}$	0.51	1	0.67
e (2σ upper limit)	<0.172	<0.095	<0.065
e (3σ upper limit)	<0.263	<0.148	<0.092
ω (°)	-59^{+132}_{-47}	21^{+59}_{-94}	65.0^{+50}_{-122}
$e\cos\omega$	$0.003^{+0.023}_{-0.018}$	$0.010^{+0.015}_{-0.011}$	$0.001^{+0.014}_{-0.010}$
$e\sin\omega$	$-0.011^{+0.028}_{-0.069}$	$0.003^{+0.034}_{-0.019}$	$0.008^{+0.026}_{-0.012}$
$\phi_{\mathrm{mid-occultation}}$	$0.502^{+0.015}_{-0.012}$	$0.5061^{+0.0096}_{-0.0067}$	$0.5007^{+0.0087}_{-0.0066}$
T_{58} (d)	$0.0915^{+0.0049}_{-0.0093}$	$0.0711^{+0.0055}_{-0.0073}$	$0.07008^{+0.00089}_{-0.00104}$
$T_{56} \approx T_{78}$ (d)	$0.0132^{+0.0033}_{-0.0030}$	>0.0257	$0.0184^{+0.0029}_{-0.0018}$
M_* ($\mathrm{M}_\odot$)	0.948 ± 0.034	0.910 ± 0.060	0.957 ± 0.034
R_* ($\mathrm{R}_\odot$)	$0.892^{+0.085}_{-0.097}$	$0.950^{+0.093}_{-0.074}$	0.928 ± 0.034
ρ_* ($\rho_\odot$)	$1.33^{+0.54}_{-0.30}$	1.06 ± 0.27	1.20 ± 0.12
M_{pl} (M_{Jup})	$0.893^{+0.071}_{-0.066}$	1.005 ± 0.053	2.100 ± 0.073
R_{pl} (R_{Jup})	$1.09^{+0.13}_{-0.14}$	$1.17^{+0.28}_{-0.14}$	1.327 ± 0.058
ρ_{pl} (ρ_{Jup})	$0.69^{+0.37}_{-0.20}$	0.64 ± 0.30	0.90 ± 0.12

This table demonstrates the effects of fitting for orbital eccentricity and is to be compared with Table 6, which presents our adopted solutions.

affected when imposing a circular orbit. The best-fitting values and associated uncertainties from MCMCs fitting an eccentric model are given in Table 5, and these are to be compared with the values of our adopted solutions in Table 6, derived using a circular model. For each system, the best-fitting eccentricity is small and the fit has a slight improvement. The parameter values of the circular and eccentric models agree to well within 1σ, and the associated uncertainties of the eccentric model are only fractionally larger.

5 ROTATIONAL MODULATION

We analysed the WASP light curves of each star to determine whether they show periodic modulation due to the combination of magnetic activity and stellar rotation. We used the sine-wave fitting method described in Maxted et al. (2011) to calculate periodograms such as those shown in the upper panels of Fig. 8. These are calculated over 4096 uniformly spaced frequencies from 0 to 1.5 cycles $\mathrm{d^{-1}}$. The false alarm probability levels shown in these figures are calculated using a bootstrap Monte Carlo method also described in Maxted et al. (2011). Variability due to star spots is not expected to be coherent on long time-scales as a consequence of the finite lifetime of star spots and differential rotation in the photosphere so we analysed each season of data separately.

We found no evidence of rotational modulation in any of the WASP-44 or WASP-45 light curves.

We applied the sine-wave fitting method to the WASP-46 light curves from each of the three seasons to produce the periodograms in the upper panels of Fig. 8. The peaks in the periodograms for the first two seasons of data are highly significant and imply periods of 16.55 ± 0.10 and 14.92 ± 0.07 d. We used a bootstrap Monte Carlo method to estimate the errors on these periods. The periodogram for the third season of data shows peaks corresponding to a period of 8.08 d. Our bootstrap Monte Carlo method fails to provide a reliable error estimate for this less significant peak. The amplitudes of the variations estimated from the sine-wave fits are in the range of 3–5 mmag (Fig. 8, lower panels). We also calculated periodograms of two stars with similar magnitudes and colours to WASP-46 observed simultaneously with the same camera. Neither of these stars showed significant periodic modulation in the same frequency interval with the exception of one season of data for one star that showed significant power close to 1 cycle $\mathrm{d^{-1}}$, the source of which is likely to be diurnal.

Table 6. System parameters from RV and transit data from our adopted, circular solutions.

Parameter (unit)	WASP-44	WASP-45	WASP-46
P (d)	2.423 8039 ± 0.000 0087	3.126 0876 ± 0.000 0035	1.430 3700 ± 0.000 0023
T_0 (HJD, UTC)	245 5434.376 ± 0.000 40	245 5441.269 25 ± 0.000 58	245 5392.315 53 ± 0.000 20
T_{14} (d)	0.0936 ± 0.0022	0.0746 ± 0.0035	0.069 73 ± 0.000 90
$T_{12} = T_{34}$ (d)	0.0146 ± 0.0026	>0.0270	0.0178 ± 0.0013
a/R_*	$8.05^{+0.66}_{-0.52}$	9.22 ± 0.74	5.74 ± 0.15
${R_{\mathrm{pl}}}^2/{R_*}^2$	0.015 88 ± 0.000 76	0.014 95 ± 0.000 71	0.021 55 ± 0.000 49
b	$0.560^{+0.076}_{-0.123}$	$0.888^{+0.045}_{-0.026}$	0.737 ± 0.019
i (°)	$86.02^{+1.11}_{-0.86}$	$84.47^{+0.54}_{-0.79}$	82.63 ± 0.38
K_1 ($\mathrm{m\,s^{-1}}$)	138.8 ± 9.0	148.3 ± 4.1	387 ± 10
γ ($\mathrm{m\,s^{-1}}$)	−4 043.82 ± 0.71	4 549.95 ± 0.63	−3 778.3 ± 1.1
e	0 (adopted)	0 (adopted)	0 (adopted)
$\mathrm{rms}_{\mathrm{spec}}$ ($\mathrm{m\,s^{-1}}$)	25.0	9.7	34.2
χ^2_{spec}	10.9	7.4	19.2
M_* ($\mathrm{M}_\odot$)	0.951 ± 0.034	0.909 ± 0.060	0.956 ± 0.034
R_* ($\mathrm{R}_\odot$)	$0.927^{+0.068}_{-0.074}$	$0.945^{+0.087}_{-0.071}$	0.917 ± 0.028
$\log g_*$ (CGS)	$4.481^{+0.068}_{-0.057}$	$4.445^{+0.065}_{-0.075}$	4.493 ± 0.023
ρ_* ($\rho_\odot$)	$1.19^{+0.32}_{-0.22}$	$1.08^{+0.27}_{-0.24}$	1.24 ± 0.10
T_{eff} (K)	5410 ± 150	5140 ± 200	5620 ± 160
[Fe/H]	0.06 ± 0.10	—	−0.37 ± 0.13
M_{pl} (M_{Jup})	0.889 ± 0.062	1.007 ± 0.053	2.101 ± 0.073
R_{pl} (R_{Jup})	1.14 ± 0.11	$1.16^{+0.28}_{-0.14}$	1.310 ± 0.051
$\log g_{\mathrm{pl}}$ (CGS)	$3.197^{+0.094}_{-0.082}$	$3.23^{+0.11}_{-0.19}$	3.447 ± 0.033
ρ_{pl} (ρ_{Jup})	$0.61^{+0.23}_{-0.15}$	0.64 ± 0.30	0.94 ± 0.11
a (au)	0.034 73 ± 0.000 41	0.040 54 ± 0.000 90	0.024 48 ± 0.000 28
$T_{\mathrm{pl},A=0}$ (K)	1343 ± 64	1198 ± 69	1654 ± 50

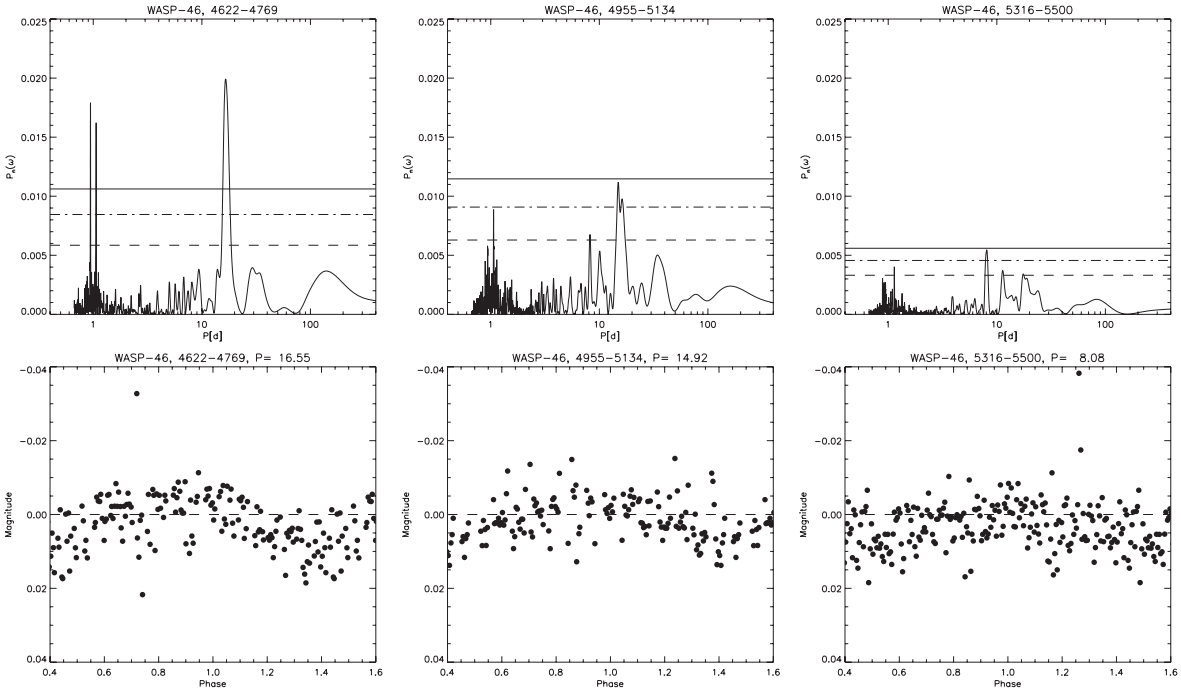

Figure 8. Upper panels: periodograms for the WASP data from three seasons for WASP46. The date range (JD −245 000) is given in the title of each panel. Horizontal lines indicate false alarm probability levels FAP = 0.1, 0.01 and 0.001. Lower panels: data folded and binned in 0.005 phase bins for the periods noted alongside the date range in the plot title.

Our interpretation of these results is that the WASP light curve of WASP-46 does show periodic modulation due to the rotation of the star with a period of 16 ± 1 d. The period of 8.08 days derived from the third season of data can be explained by the distribution of star spots during this season resulting in a light curve with two minima per cycle. Similarly, the poorly defined peak in the periodogram for the second season of data may be due to the appearance and disappearance of star spot groups during the observing season.

Using the rotational-modulation period of 16 ± 1 d and the stellar radius from Table 6, we calculate the stellar rotation velocity v to be 2.9 ± 0.2 km s^{-1}. That this value is higher than the value of $v \sin I$ (1.9 ± 1.2 km s^{-1}) determined from spectral line profiles (Section 3) suggests that the stellar spin axis is inclined by $I = 41^{\circ}{}^{+40^{\circ}}_{-27^{\circ}}$ with respect to the sky plane. This should be appreciated when assessing whether a measurement of WASP-46b's Rossiter–McLaughlin effect is indicative of an aligned or a misaligned orbit (e.g. Schlaufman 2010). Usually only the sky-projected angle between the planetary orbit and stellar spin axis can be determined, but with a measurement of I the true angle can be determined. Our measurement of I is imprecise and would be improved by a more precise determination of spectroscopic $v \sin I$.

6 DISCUSSION

WASP-44b is a 0.89-$M_{\rm Jup}$ planet in a 2.42-d orbit around a solar metallicity ([Fe/H] = 0.06 ± 0.10) G8V star. The star is observable from both hemispheres and seems to be inactive as it shows no signs of rotational modulation or Ca II H+K emission.

WASP-45b is a Jupiter-mass planet that partially transits its metal-rich ([Fe/H] = 0.36 ± 0.12) K2V host star every 3.13 d. The (near-)grazing nature of the transits led us to impose a prior on the density of the host star so that the derived stellar and planetary radii are physical. The star may be active as weak Ca II H+K emission is seen in its spectra, though no rotational modulation is evident in the light curves.

WASP-46b is a 2.10-$M_{\rm Jup}$ planet in a 1.43-d orbit around a metal-poor ([Fe/H] = −0.37 ± 0.13) G6V star. We found the star to be active as weak Ca II H+K emission is present in its spectra and a clear 16-day rotational-modulation signature is evident in the WASP light curves. The slower rotation rate suggested by spectroscopic $v \sin I$ indicates that the stellar spin axis is inclined relative to the sky plane ($I = 41^{\circ} \pm 40^{\circ}$). By observing WASP-46b's Rossiter–McLaughlin effect (e.g. Simpson et al. 2011), which is predicted to have an amplitude of 18 m s^{-1}, we could thus measure the true angle between the stellar spin and the planetary orbit axes, rather than just the sky-projected angle. The large size of the planet, the high stellar insolation and the relative lateness of the host star make WASP-46b a good target for infrared occultation photometry (e.g. Anderson et al. 2011b).

The upper limits placed on the lithium abundances suggest that each star is at least a few Gyr old (Table 3; Sestito & Randich 2005), which is in contrast with the gyrochronological ages of ∼0.9–1.4 Gyr.

6.1 Fit for eccentricity or impose a circular orbit

To obtain accurate stellar densities and the derivative stellar and planetary radii, we require not only high-quality transit light curves, but also accurate determinations of the orbital eccentricities. Measurements of these parameters inform intense theoretical efforts concerning tidal circularization and heating, bulk planetary composition and the observed systematic errors in planetary and stellar radii. For those planets with poorly constrained eccentricity, further RV and occultation-timing measurements are necessary. However, these will be performed slowly and perhaps only for a fraction of systems. As such, we should make every effort to avoid introducing biases into the sample that we have to work with.

Around half of all known transiting planets (i.e. those confirmed by a dynamical mass determination) are hot Jupiters ($P \lesssim 4$ d and $M_{\rm pl} \approx 0.5$–$2\ M_{\rm Jup}$) and Pont et al. (2011) find no evidence for an eccentric orbit among these. Further, tidal theory predicts that the time-scale of tidal circularization is a sharp function of semimajor axis and planet radius, and a weaker function of planetary and stellar masses (Goldreich & Soter 1966). That is, low-mass, bloated planets in short orbits around high-mass stars are expected to circularize quickest. So, there is a theoretical basis and an empirical basis for expecting a newly discovered hot Jupiter to be in a circular orbit.

When a hot Jupiter is first announced the RV data often poorly constrain eccentricity and occultation observations are almost never available. In those circumstances, some authors have opted to impose a circular orbit (e.g. Anderson et al. 2011a; Faedi et al. 2011a), as is theoretically and empirically reasonable, though doing so does artificially reduce the uncertainties on the system parameters. Other authors have opted to fit for an eccentric orbit (e.g. Hellier et al. 2010; Bakos et al. 2011) so as to obtain more conservative error bars. Fitting an eccentric orbit model to RV measurements of a (near-)circular orbit will always result in a non-zero value of e (e.g. Laughlin et al. 2005), and this can affect the derived stellar and planetary parameters. As compared to the circular solution, the eccentric solution will typically change the planet's speed during transit and, as the transit duration is fixed by measurement, a change in speed necessitates a change in distance travelled during transit, i.e. the derived stellar radius. In turn, as the ratio of planetary-to-stellar radii is fixed by the measured transit depth, then the derived planet radius is changed.

Being aware of these issues, some authors have opted to present both a circular solution, which is most likely, and an eccentric solution, which gives a reliable account of the uncertainties in the data (e.g. Anderson et al. 2010). One issue with this approach is that many authors tend to prefer to work with a single solution and so will adopt the one they favour regardless. Another approach is to present the best-fitting parameter values from a circular fit and the error bars from an eccentric fit (e.g. Enoch et al. 2011; Maxted et al. 2011). Thus, the most likely solution is presented with conservative error bars, but care must be taken to calculate the 1σ confidence intervals in the posterior probability distributions about the best-fitting circular values.

As the best-fitting eccentricity values for the three systems presented in this paper are small ($e = 0.02$–0.04), the differences between the best-fitting parameter values from circular and eccentric solutions are small (compare Tables 5 and 6). However, eccentricity is often poorly determined in a discovery paper and the choice to fit for eccentricity then has a greater impact. An illustrative example is the case of WASP-17b. In the discovery paper (Anderson et al. 2010), we presented three solutions, including one with an imposed circular orbit which gave $R_{\rm pl} = 1.97 \pm 0.10\ R_{\rm Jup}$, and another, which we adopted as our preferred solution, in which we fit for an eccentric orbit that gave $R_{\rm pl} = 1.74^{+0.26}_{-0.23}\ R_{\rm Jup}$ and $e = 0.129^{+0.106}_{-0.068}$. We had initially favoured the circular solution as theory suggested this as the most likely and the additional two free parameters of an eccentric orbit did not significantly improve the fit. However, we adopted the eccentric solution due to its more conservative error bars. We had been able to place only a weak constraint on eccentricity as the low mass of the planet ($0.49\ M_{\rm Jup}$) and the high effective surface temperature of the star (6650 K) caused our measurement of the reflex motion of the star to be quite low S/N. This situation improved when we observed two occultations of WASP-17b, which we used to show the orbit of WASP-17b to be very slightly eccentric ($e \approx 0.0055$; Anderson et al. 2011b) and the planet radius to be $1.991 \pm 0.081\ R_{\rm Jup}$. As such, the circular solution that we presented in the discovery paper was closest to describing the system and we would have done better to have adopted that.

By the time we had shown the orbit of WASP-17b to be near-circular, a number of papers had, at least in part, based their models, results or conclusions on the values of one or both of e and $R_{\rm pl}$ of the discovery paper's adopted solution (e.g. Hansen 2010; Schlaufman 2010; Cowan & Agol 2011; Ehrenreich & Désert 2011). Though it is true that our updated solution was not excluded, not even at the 1σ level, some of those studies had only considered WASP-17 due to its apparent significant eccentricity, and other such works were sure to follow. For example, the possibility that tidal dissipation could have inflated WASP-17b would probably have been tested as was done by Ibgui et al. (2011) for other systems. Before we showed the planet to be even more bloated than first suggested and placed a much tighter constraint on eccentricity, tidal heating had seemed a much more likely explanation for the anomalously large size of WASP-17b.

A more recent example, which is similar to the case of WASP-17 and became available after submission of this paper, is that of HAT-P-32 and HAT-P-33 (Hartman et al. 2011). In both systems, the S/N of the stellar radial motion, as induced by the orbiting planet, is low and eccentricity is poorly constrained. In an early draft (arXiv:1106.1212v1), eccentric solutions were presented alongside circular solutions such that the reader could choose which to adopt. The derived planetary radii differ significantly between the eccentric and circular solutions, with 1.8 $R_{\rm Jup}$ versus 2.0 $R_{\rm Jup}$ for HAT-P-32b and 1.7 $R_{\rm Jup}$ versus 1.8 $R_{\rm Jup}$ for HAT-P-33b. In the published version of the paper, Hartman et al. (2011) instead suggest adoption of the circular solutions, but caution that several eccentric short-period planets are known. The three example exoplanets given, XO-3b, WASP-14b and HAT-P-21b, are each much more massive and smaller than HAT-P-32b and HAT-P-33b, and are in similar or longer orbits. Each effect acts to increase the tidal circularization time-scale. Thus, it is little wonder that these planets are in eccentric orbits, but it would be surprising if HAT-P-32b or HAT-P-33b were.

Unless there is clear evidence for an eccentric orbit, we recommend imposing a circular orbit when deriving the parameters of a hot-Jupiter system. This will avoid creep in the literature of parameter values as further RV and occultation observations show discovery-paper eccentricities to be spurious. Though further measurements will show some planets to have a small, non-zero eccentricity, for the majority eccentricity will be constrained to ever smaller values consistent with zero.

ACKNOWLEDGMENTS

WASP-South is hosted by the South African Astronomical Observatory and SuperWASP-N is hosted by the Issac Newton Group on La Palma. We are grateful for their ongoing support and assistance. Funding for WASP comes from consortium universities and from the UK's Science and Technology Facilities Council. TRAPPIST is a project funded by the Belgian Fund for Scientific Research (Fond National de la Recherche Scientifique, FNRS) under the grant FRFC 2.5.594.09.F, with the participation of the Swiss National Science Foundation (SNF). MG and EJ are FNRS Research Associates.

REFERENCES

Anderson D. R. et al., 2010, ApJ, 709, 159
Anderson D. R. et al., 2011a, A&A, 531, A60
Anderson D. R. et al., 2011b, MNRAS, 416, 2108

Bakos G. Á. et al., 2011, ApJ, 742, 116
Baranne A. et al., 1996, A&AS, 119, 373
Barnes S. A., 2007, ApJ, 669, 1167
Bodenheimer P., Lin D. N. C., Mardling R. A., 2001, ApJ, 548, 466
Bruntt H. et al., 2010, MNRAS, 405, 1907
Claret A., 2000, A&A, 363, 1081
Claret A., 2004, A&A, 428, 1001
Collier Cameron A. et al., 2006, MNRAS, 373, 799
Collier Cameron A. et al., 2007, MNRAS, 380, 1230
Cowan N. B., Agol E., 2011, ApJ, 726, 82
Demarque P., Woo J.-H., Kim Y.-C., Yi S. K., 2004, ApJS, 155, 667
Ehrenreich D., Désert J.-M., 2011, A&A, 529, A136
Enoch B., Collier Cameron A., Parley N. R., Hebb L., 2010, A&A, 516, A33
Enoch B. et al., 2011, MNRAS, 410, 1631
Faedi F. et al., 2011a, A&A, 531, A40
Faedi F. et al., 2011b, in Bouchy F., Díaz R., Moutou C., eds, Detection and Dynamics of Transiting Exoplanets. St Michel l'Observatoire, France (EPJ Web Conf., 11, 01003)
Fortney J. J., Marley M. S., Barnes J. W., 2007, ApJ, 659, 1661
Gillon M. et al., 2009, A&A, 501, 785
Gillon M., Jehin E., Magain P., Chantry V., Hutsemékers D., Manfroid J., Queloz D., Udry S., 2011, in Bouchy F., Díaz R., Moutou C., eds, Detection and Dynamics of Transiting Exoplanets. St Michel l'Observatoire, France (EPJ Web Conf., 11, 06002)
Goldreich P., Soter S., 1966, Icarus, 5, 375
Hansen B. M. S., 2010, ApJ, 723, 285
Hartman J. D. et al., 2011, ApJ, 742, 59
Hellier C. et al., 2010, ApJ, 723, L60
Hellier C. et al., 2011, in Bouchy F., Díaz R., Moutou C., eds, Detection and Dynamics of Transiting Exoplanets. St Michel l'Observatoire, France (EPJ Web Conf., 11, 01004)
Ibgui L., Spiegel D. S., Burrows A., 2011, ApJ, 727, 75
Laughlin G., Marcy G. W., Vogt S. S., Fischer D. A., Butler R. P., 2005, ApJ, 629, L121
Lucy L. B., Sweeney M. A., 1971, AJ, 76, 544
Magain P., 1984, A&A, 134, 189
Mandel K., Agol E., 2002, ApJ, 580, L171
Maxted P. F. L. et al., 2011, PASP, 123, 547
Pepe F. et al., 2005, The Messenger, 120, 22
Pollacco D. L. et al., 2006, PASP, 118, 1407
Pollacco D. et al., 2008, MNRAS, 385, 1576
Pont F., Husnoo N., Mazeh T., Fabrycky D., 2011, MNRAS, 414, 1278
Queloz D. et al., 2000, A&A, 354, 99
Queloz D. et al., 2001, A&A, 379, 279
Queloz D. et al., 2010, A&A, 517, L1
Schlaufman K. C., 2010, ApJ, 719, 602
Seager S., Mallén-Ornelas G., 2003, ApJ, 585, 1038
Sestito P., Randich S., 2005, A&A, 442, 615
Simpson E. K. et al., 2011, MNRAS, 414, 3023
Skrutskie M. F. et al., 2006, AJ, 131, 1163
Stetson P. B., 1987, PASP, 99, 191
Torres G., Andersen J., Giménez A., 2010, A&AR, 18, 67

SUPPORTING INFORMATION

Additional Supporting Information may be found in the online version of this article.

Table 2. Euler and TRAPPIST photometry of the three stars.

Please note: Wiley-Blackwell are not responsible for the content or functionality of any supporting materials supplied by the authors. Any queries (other than missing material) should be directed to the corresponding author for the article.

This paper has been typeset from a TEX/LATEX file prepared by the author.